IV International Conference on Particle-based Methods – Fundamentals and Applications
PARTICLES 2015
E. Oñate, M. Bischoff, D.R.J. Owen, P. Wriggers & T. Zohdi (Eds)

ADAPTIVE REFINEMENT TECHNIQUE FOR DISCRETE STATIC MODELS OF FRACTURE

JAN ELIÁŠ

Brno University of Technology, Faculty of Civil Engineering
Veveří 331/95, Brno, 60200, Czech Republic
elias.j@fce.vutbr.cz, http://www.fce.vutbr.cz/STM/elias.j/

Key words: discrete model, random geometry, statics, adaptivity, discretization, concrete

Abstract. The discrete static models are advantageneously used for fracture simulations in heterogeneous materails. These simulations are often extremely computationally demanding. The contribution aims to reduction of computationa cost via adaptivity in construction of the discrete model geometry. The simulation starts with coarse discretization that provides correct elastic behavior; the discretization is adaptively refined during the simulation in regions that suffer high stresses.

1 INTRODUCTION

Discrete representation of materials is a natural alternative to continuous approaches. A collection of interconnected rigid cells organized into a net structure is often called discrete or lattice model. Lattice models are being used in several versions; we focus here only on static models with lattices of random geometry based on Voronoi tessellation, such as [1, 2, 3].

The fine discretization of the discrete model leads to extreme computational demands, but it is often necessary; especially when it is related to meso-scale structure of the simulated material. The contribution presents a technique to adaptively refine model discretization. Without this tool, it is necessary to densely discretize the whole domain and therefore to create computationally demanding model. Availability of adaptive refinement allows starting simulation with coarse discretization and refining it adaptively during simulation run.

Successful attempts to introduce this important feature already exist [4, 5]. They are based on adaptive replacement of some continuous model with the discrete one, but problematic interface between continuum and discrete model is involved and the discrete model has to have regular geometry (that produces directional bias).

Another approach is proposed here. The adaptive refinement is performed within the discrete lattice model only and allows using irregular geometry based on Voronoi

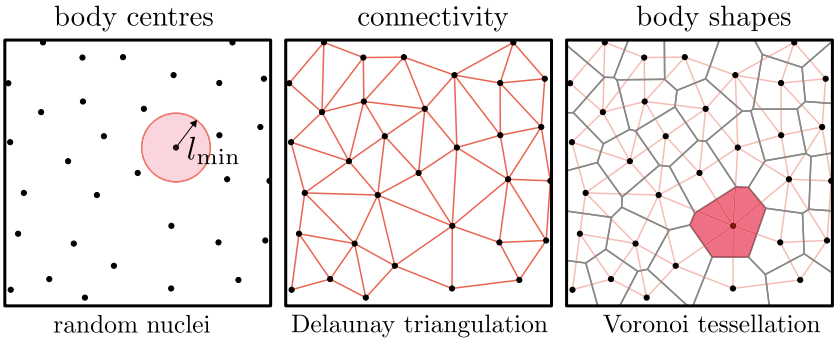

Figure 1: Model geometry obtained by Voronoi tessellation on randomly placed nuclei with restricted minimum distance $l_{\min}$, 2D sketch.

tessellation. The algorithm works as follows. Initially, the whole domain is coarsely discretized. Whenever any region of the coarse model exceeds some criterion based on the equivalent stress, the coarse discretization in its vicinity is replaced by the finer one and some transitional area connecting the coarse and fine discretization is inserted around. The rest of the domain discretization will remain the same. Finally, comparison of adaptively discretized and fully densely discretized models is presented.

2 RANDOM GEOMETRY OF THE MODEL

The model geometry is random to avoid directional bias that occur in any regular structure. Domain of the modeled element is filled by nuclei with randomly generated positions. These nuclei are added sequentially and accepted only when distances to previously placed nuclei are greater than chosen parameter $l_{\min}$, see Fig. 1. The parameter $l_{\min}$ controls discretization density and therefore it should correspond to the size of heterogeneities in the material (e.g. aggregate diameter). Varying discretization density in the model can be achieved by spatial varying the parameter $l_{\min}$. Each of the nuclei will serve as center of one rigid body and three translational $\boldsymbol{u}$ and three rotational $\boldsymbol{\theta}$ degrees of freedom (DOF) will be associated with it.

The domain is considered as saturated by nuclei when new nucleus is rejected for large number of subsequent trials. Delaunay triangulation that provides connectivity between the nuclei is performed. Dual diagram of Voronoi tessellation then provides geometry of the rigid bodies, see Fig. 1. Rigid bodies has common contact facets that are perpendicular to their connections; facet centroids are denoted $\boldsymbol{c}$, see Fig. 2.

3 LINEAR ELASTIC BEHAVIOR

The elastic behavior of the discrete system is *independent* on discretization density. This statement is fundamental assumption of the adaptive technique, but it is not obvious. The proof and numerical verification is delivered here.

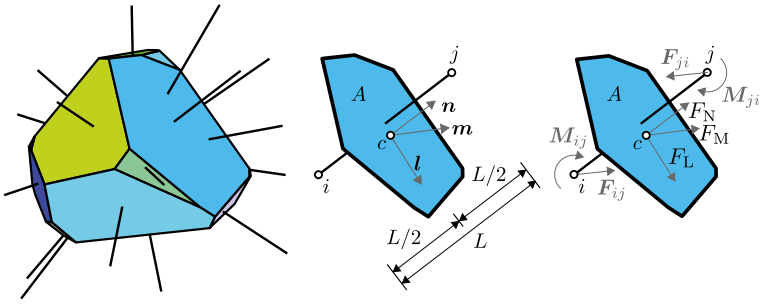

Figure 2: One discrete body of random geometry and one contact facet between nuclei i and j - normal and tangential directions and forces.

3.1 Scaling of elastic problem

This section is based on work [6], from which it adopts both notation and theory.

Let us analyze one contact between nuclei i and j of coordinates $\boldsymbol{x}_i = [x_{1i}, x_{2i}, x_{3i}]^T$ and $\boldsymbol{x}_j$ with central point $\boldsymbol{c}$, elastic modulus E and lenght L, see Fig. 2. The translations of point i are denoted $\boldsymbol{u}_i = [u_{1i}, u_{2i}, u_{3i}]^T$ and rotations are $\boldsymbol{\theta}_i = [\theta_{1i}, \theta_{2i}, \theta_{3i}]^T$. Then from rigid body motion (assuming small rotations), position of any point $\boldsymbol{x}$ inside the body associated with nucleus i can be expressed as

$$\boldsymbol{u}(\boldsymbol{x}) = \boldsymbol{u}_i + \boldsymbol{\theta}_i \times (\boldsymbol{x} - \boldsymbol{x}_i) = \boldsymbol{A}_i(\boldsymbol{x}) \begin{bmatrix} \boldsymbol{u}_i \\ \boldsymbol{\theta}_i \end{bmatrix} \tag{1}$$

with matrix $\boldsymbol{A}_i(\boldsymbol{x})$ being

$$\boldsymbol{A}_i(\boldsymbol{x}) = \begin{bmatrix} 1 & 0 & 0 & 0 & x_3 - x_{3i} & x_{2i} - x_2 \\ 0 & 1 & 0 & x_{3i} - x_3 & 0 & x_1 - x_{1i} \\ 0 & 0 & 1 & x_2 - x_{2i} & x_{1i} - x_1 & 0 \end{bmatrix} \tag{2}$$

Displacement jump $\boldsymbol{\Delta}_{ij}$ between bodies i and j is measured by their separation at common facet centroid $\boldsymbol{c}$. Therefore, it can be expressed as

$$\boldsymbol{\Delta}_{ij} = \begin{bmatrix} \Delta_{1ij} & \Delta_{2ij} & \Delta_{3ij} \end{bmatrix}^T = \boldsymbol{A}_j(\boldsymbol{c}) \begin{bmatrix} \boldsymbol{u}_j \\ \boldsymbol{\theta}_j \end{bmatrix} - \boldsymbol{A}_i(\boldsymbol{c}) \begin{bmatrix} \boldsymbol{u}_i \\ \boldsymbol{\theta}_i \end{bmatrix} \tag{3}$$

Based on displacement jumps, contact forces are calculated. Three contact forces acting at point $\boldsymbol{c}$ in normal direction, $\boldsymbol{n}$, and two tangential directions, $\boldsymbol{m}$ and $\boldsymbol{l}$, are given by

$$\boldsymbol{F} = \begin{bmatrix} F_N & F_M & F_L \end{bmatrix}^T = \begin{bmatrix} \dfrac{\boldsymbol{n}^T \boldsymbol{\Delta}_{ij} EA}{L} & \dfrac{\boldsymbol{m}^T \boldsymbol{\Delta}_{ij} \alpha EA}{L} & \dfrac{\boldsymbol{l}^T \boldsymbol{\Delta}_{ij} \alpha EA}{L} \end{bmatrix}^T \tag{4}$$

Model parameter α controls the macro-scopic Poisson's ratio.

Forces and moments acting on nuclei i ($\boldsymbol{F}_{ij}$ and $\boldsymbol{M}_{ij}$) and j ($\boldsymbol{F}_{ji}$ and $\boldsymbol{M}_{ji}$) due to contact ij can be obtained from principle of virtual work

$$\begin{bmatrix} \boldsymbol{F}_{ij} \\ \boldsymbol{M}_{ij} \end{bmatrix}^T \begin{bmatrix} \delta\boldsymbol{u}_i \\ \delta\boldsymbol{\theta}_i \end{bmatrix} + \begin{bmatrix} \boldsymbol{F}_{ji} \\ \boldsymbol{M}_{ji} \end{bmatrix}^T \begin{bmatrix} \delta\boldsymbol{u}_j \\ \delta\boldsymbol{\theta}_j \end{bmatrix} = \begin{bmatrix} F_N \\ F_M \\ F_L \end{bmatrix}^T \begin{bmatrix} \boldsymbol{n}^T\delta\boldsymbol{\Delta}_{ij} \\ \boldsymbol{m}^T\delta\boldsymbol{\Delta}_{ij} \\ \boldsymbol{l}^T\delta\boldsymbol{\Delta}_{ij} \end{bmatrix} \tag{5}$$

where δ denotes the virtual quantities. Substitution of equation (3) provides

$$\begin{bmatrix} \boldsymbol{F}_{ij} \\ \boldsymbol{M}_{ij} \end{bmatrix}^T = -F_N\boldsymbol{n}^T\boldsymbol{A}_i(c) - F_M\boldsymbol{m}^T\boldsymbol{A}_i(c) - F_L\boldsymbol{l}^T\boldsymbol{A}_i(c) \tag{6}$$

$$\begin{bmatrix} \boldsymbol{F}_{ji} \\ \boldsymbol{M}_{ji} \end{bmatrix}^T = F_N\boldsymbol{n}^T\boldsymbol{A}_j(c) + F_M\boldsymbol{m}^T\boldsymbol{A}_j(c) + F_L\boldsymbol{l}^T\boldsymbol{A}_j(c) \tag{7}$$

The equilibrium must be achieved in every nuclei when contribution from all contacts and external forces are summarized.

Now, what happen when the whole problem is scaled in all three dimensions by factor ξ. Then, coordinates, contact lengths and areas becomes $\overline{\boldsymbol{x}} = \xi\boldsymbol{x}$, $\overline{L} = \xi L$ and $\overline{A} = \xi^2 A$. The matrix $\overline{\boldsymbol{A}}$ has now form

$$\overline{\boldsymbol{A}}_i(\boldsymbol{x}) = \begin{bmatrix} 1 & 0 & 0 & 0 & \xi\,(x_3 - x_{3i}) & \xi\,(x_{2i} - x_2) \\ 0 & 1 & 0 & \xi\,(x_{3i} - x_3) & 0 & \xi\,(x_1 - x_{1i}) \\ 0 & 0 & 1 & \xi\,(x_2 - x_{2i}) & \xi\,(x_{1i} - x_1) & 0 \end{bmatrix} \tag{8}$$

To induce the same stress level in the scaled domain, the external force load must scale with the same factor ($\overline{\boldsymbol{F}}_{\mathrm{e}} = \xi^2\boldsymbol{F}_{\mathrm{e}}$) as areas. We now search for displacements and rotations $\overline{\boldsymbol{u}}$ and $\overline{\boldsymbol{\theta}}$ that satisfy equilibrium in all nuclei.

Apparently, the unknown DOF are $\overline{\boldsymbol{u}} = \xi\boldsymbol{u}$ and $\overline{\boldsymbol{\theta}} = \boldsymbol{\theta}$, i.e. translations are linearly scaled and rotations remains unchanged. Plugging this solution into Eqs. (6) and (7), the nodal forces are scaled with ξ^2 while the moments with ξ^3. The nodal equilibrium then yields

$$\overline{\boldsymbol{F}}_{\mathrm{e}} + \sum_j \overline{\boldsymbol{F}}_{ij} = \xi^2\left(\boldsymbol{F}_{\mathrm{e}} + \sum_j \boldsymbol{F}_{ij}\right) = \boldsymbol{0} \tag{9}$$

$$\overline{\boldsymbol{M}}_{\mathrm{e}} + \sum_j \overline{\boldsymbol{M}}_{ij} = \xi^3\left(\boldsymbol{M}_{\mathrm{e}} + \sum_j \boldsymbol{M}_{ij}\right) = \boldsymbol{0} \tag{10}$$

based on equilibrium achieved in the original unscaled problem.

Let us now estimate the macro-scopic elastic modulus $\tilde{E}$ and Poisson's ratio ν. These two variables relates the stresses and strains in the structure. Since both stresses (forces scaled with ξ^2 over areas scaled with ξ^2 as well) and strains (deformations scaled with ξ over length scaled with ξ as well) remain unchanged, also the elastic modulus and Poisson's ratio on discretization with $\bar{l}_{\min} = \xi l_{\min}$ are constant for arbitrary ξ.

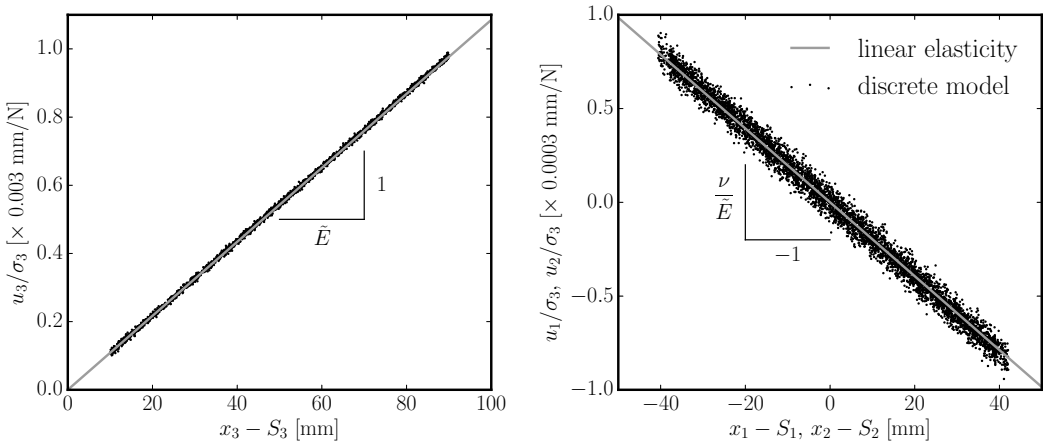

Figure 3: Estimation of macro-scopic elastic constants via least square fitting of deformation field.

3.2 Numerical verification

The analytically derived conclusion is verified numerically here. Volume $100\times100\times100\,\mathrm{mm}^3$ is compressed by low level stress σ_3 in z direction. Assuming ideally homogeneous material, constant stress over the whole domain with the only nonzero component σ_3 is obtained and the strain field is constant as well having three nonzero components

$$\left[\begin{array}{ccc} \varepsilon_1 & \varepsilon_2 & \varepsilon_3 \end{array}\right]^T = \frac{\sigma_3}{\tilde{E}} \left[\begin{array}{ccc} -\nu & -\nu & 1 \end{array}\right]^T \tag{11}$$

with $\tilde{E}$ and ν being the macro-scopic elastic modulus and Poisson's ratio. The deformation field can be obtained from strains

$$u_i = \varepsilon_i (x_i - S_i) \tag{12}$$

with $i \in \{1, 2, 3\}$ being the Cartesian coordinates and S_i coordinates of a point that preserves constant position during loading. The point $\boldsymbol{S}$ is typically known from the boundary conditions.

Combining Eqs. (11) and (12), the following equalities hold

$$\frac{u_1}{\sigma_3} = -\frac{\nu}{\tilde{E}}(x_1 - S_1) \qquad \frac{u_2}{\sigma_3} = -\frac{\nu}{\tilde{E}}(x_2 - S_2) \qquad \frac{u_3}{\sigma_3} = \frac{1}{\tilde{E}}(x_3 - S_3) \tag{13}$$

These equations offer simple way to determine macro-scopis elastic modulus and Poisson's ratio. Simulating the compressed cube using the discrete model, one can simply obtain deformations u_i and locations x_i. Then, least square fitting can be performed to determine the unknown elastic constants. The fitting is shown in Fig. 3. Meso-scopic elastic modulus was $E = 48\,\mathrm{GPa}$ and $\alpha = 0.29$.

Several discretization densities were tested and macro-scopic elastic parameters were fitted. The results are shown in Fig. 4 where the mean value and the standard deviation of

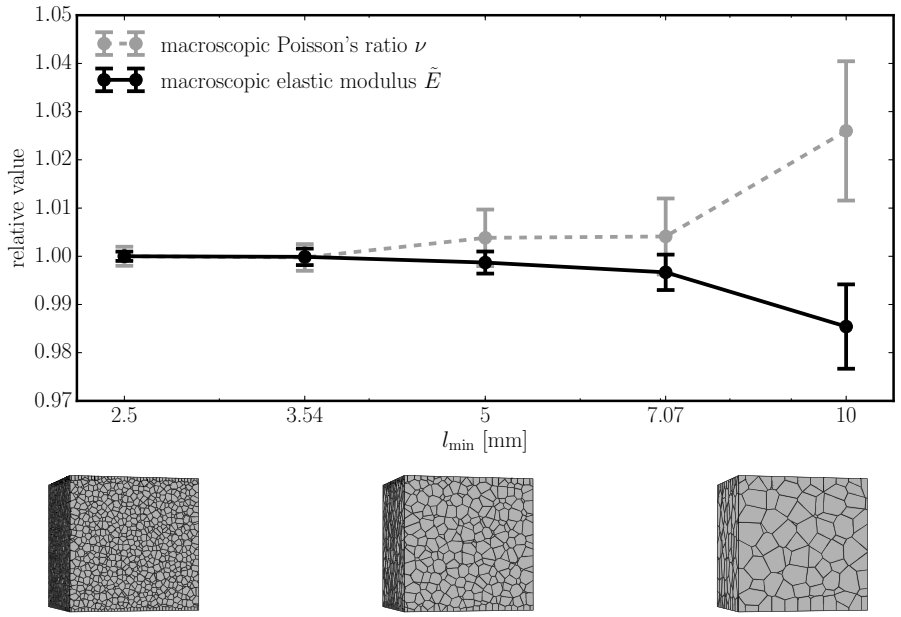

Figure 4: Elastic constants identified on discrete system with different discretization density $l_{\min}$.

relative quantity (with respect to the one obtained with smallest $l_{\min}$) from 20 realization are computed for every considered $l_{\min}$. One can see that

- the difference between values of both elastic modulus and Poisson's ratio are within $\pm 3\%$. Therefore, one can conclude that elastic behavior of the particle system is independent on discretization density.
- the standard deviation decreases with decreasing $l_{\min}$. This is because as the number of bodies in the model increases, the response becomes less sensitive to the random location of the nuclei.
- there is certain convergence pattern. This has to be attributed to the boundary effect. The rigid bodies at the boundary have slightly different shapes as they have one or more sides determined by the boundary planes. Therefore, they have slightly different elastic properties. With increasing density of the discretization, this boundary layer occupies lower portion of the volume and the effect diminishes.

Especially the last point is important. The elastic behavior is invariant with respect to $l_{\min}$ but not with respect to body shapes, e.g. anisotropic elastic behavior can be expected for bodies elongated in one direction. The discretization has to be also fine enough to account for strain gradients in the model.

4 NON-LINEAR BEHAVIOR

The nonlinear constitutive model applied at facets is based on damage parameter D ranging from 0 (healthy material) to 1 (completely damage material). The details of the

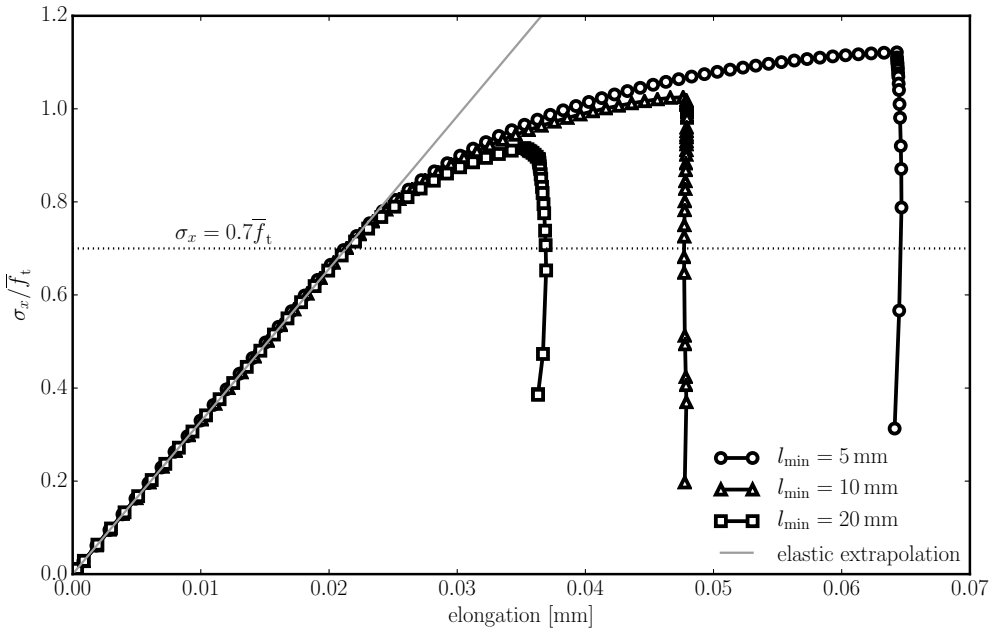

Figure 5: Response of discrete system loaded in tension.

nonlinear constitutive equations are not provided here since these are not crucial for the presented concept of adaptivity. The nonlinear behavior model is again adopted from works of Gainluca Cusatis [7, 8, 6, 9]. Fracture parameters of the model were taken from simulations [10] of large experimental series [11, 12, 13] on concrete. The meso-scopic tensile strengths in tension and shear were 2.66 MPa and 7.98 MPa, the meso-scopic fracture energies in tension and shear were $20\,\mathrm{Jm}^{-2}$ and $320\,\mathrm{Jm}^{-2}$.

Contrary to the linear elastic behavior, the nonlinear behavior of the model is *dependent* on discretization density. This is, however, understood as beneficial. The model discretization should correspond to the material heterogeneity and therefore dependence on $l_{\min}$ reflects changes in material behavior due different grain size.

Simple tension simulations were performed to investigate effect of discretization in nonlinear regime. The beam cross-section was $100\times100\,\mathrm{mm}^2$ and length was 400 mm. The relative stress in the beam is calculated as the loading force divided by cross-section area ($0.01\,\mathrm{m}^2$) and meso-level tensile strength ($f_\mathrm{t} = 2.66\,\mathrm{MPa}$). Beam elongation against the relative beam stress is plotted in Fig. 5. The finer the discretization, the higher the strength. However, until approximately 70% of the relative stress, all the models remain elastic.

5 ADAPTIVE DISCRETIZATION REFINEMENT

Two types of nuclei are distinguished. Those that belong to fine discretization region of target density $l_{\min} = l_\mathrm{f}$ and the others. Initially, the coarse discretization is performed using $l_{\min} = l_\mathrm{c}$ and all nuclei belongs to the latter group. Non-linear behavior is allowed

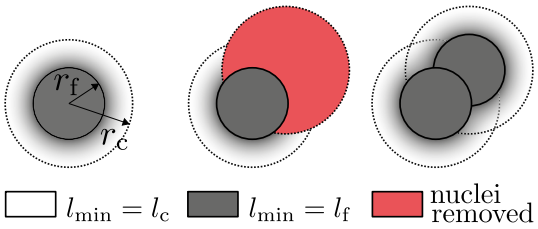

Figure 6: Adaptive refinement of discretization in steps.

only at facets connecting nuclei from the former group, any connection that involves nucleus from coarser discretization behaves linearly elastic.

The adaptive refinement of discretization is performed within sphere of radius r_c. All nuclei that belongs to this sphere but not to the fine discretization are removed. Then, new nuclei are added using the same procedure as described in Sec. 2. The parameter l_min is set to l_f inside inner sphere of radius r_f and is linearly changing with distance from the sphere center r

$$l_\mathrm{min} = \begin{cases} l_\mathrm{f} & \text{for } r < r_\mathrm{f} \\ l_\mathrm{f} + r\dfrac{l_\mathrm{c} - l_\mathrm{f}}{r_\mathrm{c} - r_\mathrm{f}} & \text{otherwise} \end{cases} \tag{14}$$

Described replacement of nuclei is schematically shown in Fig. 6. The linear transition from coarse to fine discretization is included to keep the shape of the bodies approximately the same in statistical sense. If the transitional regime is omitted, the sharp change in discretization density would produce significantly elongated body shapes, directional bias and anisotropy.

On the newly created nuclei, triangulation and tessellation is performed. New system stiffness matrix is assembled and calculation continues. The damaged connections are only between nuclei from fine discretization that were not affected by the discretization refinement and therefore all the state variables are automatically transfered to the new discrete system.

Last component of the adaptivity algorithm is the decision where and when the refinement should take place. The straightforward way would be to check all the connections from the coarse discretization and build the adaptivity criterion on the level of equivalent stress reached at the facets. This would however lead to refinement of the model in excessively many regions. Due to random discretization, some of the facet suffer high equivalent stress even under low far field stress. To identify the regions of high stress more robustly, application of some stress averaging is reasonable.

Therefore, refinement criteria is base on an average stress in rigid bodies. The fabric stress tensor can be utilized to evaluate average stress tensor components in body i

$$\sigma_{kl}^{(i)} = \frac{1}{V^{(i)}} \sum_j F_k^{(ij)} c_l^{(ij)} \tag{15}$$

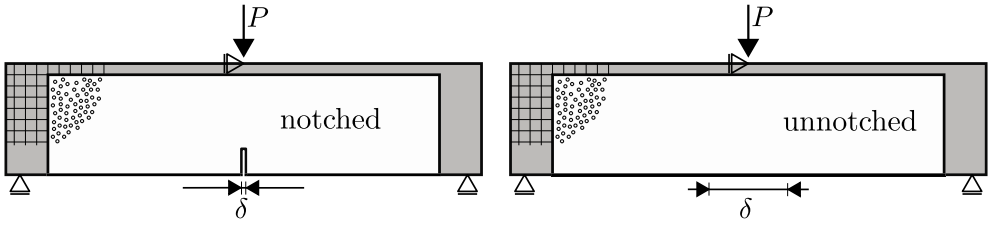

Figure 7: Beam subjected to three-point bending with notch (left) and without notch (right).

where j runs over all nuclei in contact with nucleus i; k and l are Cartesian coordinates, $\boldsymbol{F}$ is a vector of contact force and $\boldsymbol{c}$ is centroid of contact facet.

The Mazar's equivalent stress [14] serves as measure of the stress level in the body

$$\sigma_{\mathrm{eq}} = \sqrt{\sum_{p=\mathrm{I}}^{\mathrm{III}} \langle \sigma_p \rangle^2} \tag{16}$$

with $\sigma_{\mathrm{I-III}}$ being the principal stresses and $\langle \cdot \rangle$ returning the positive part of the argument. After every solution step, stress tensors in all rigid bodies belonging to coarse disretization are evaluated (Eq. (15)). Then, principal stresses and equivallent stresses (Eq. (16)) are calculated. Whenever $\sigma_{\mathrm{eq}}/f_{\mathrm{t}} > \gamma$, the discretization os adapted and the nuclei associated with that rigid body serves as a center of the refinement sphere.

The adaptivity model brings additional 4 parameters: coarse discretization density l_{c}, radii l_{c} and l_{f} and relative stress limit γ. Based on uniaxial tension simulations, reasonable limit seems to be $\gamma = 0.7$.

6 EXAMPLE

Proposed adaptive algorithm is tested on simulation of three-point bending tests. The beams had 200 mm in depth, 800 mm in span and thickness was 100 mm. Two variants were considered: notched variant with relative notch depth 0.25 and unnotched variant. The geometry of the beam as well as area where the discrete model was applied is shown in Fig. 7.

The same material parameters as in Sec. 3.2 and 4 of the model were used. Fine discretization density was set to $l_{\mathrm{f}} = 10\,\mathrm{mm}$, the coarse one was $l_{\mathrm{c}} = 20\,\mathrm{mm}$, radii of adapted region were $r_{\mathrm{f}} = 60\,\mathrm{mm}$ and $l_{\mathrm{f}} = 120\,\mathrm{mm}$, limit for refinement was kept $\gamma = 0.7$. The adaptive model response is compared with response of finely discretized model, that serves as a reference solution.

Figure 8 shows response of the reference and adaptive model for both notched (left) and unnotched (right) beams. The blue circles highlight steps where refinement was performed. In linear part and initial nonlinear part of the diagrams the adaptive and reference model coincide. However, the peak load is different. This is attributed to the randomness of the response, the models have different location of the nuclei and therefore

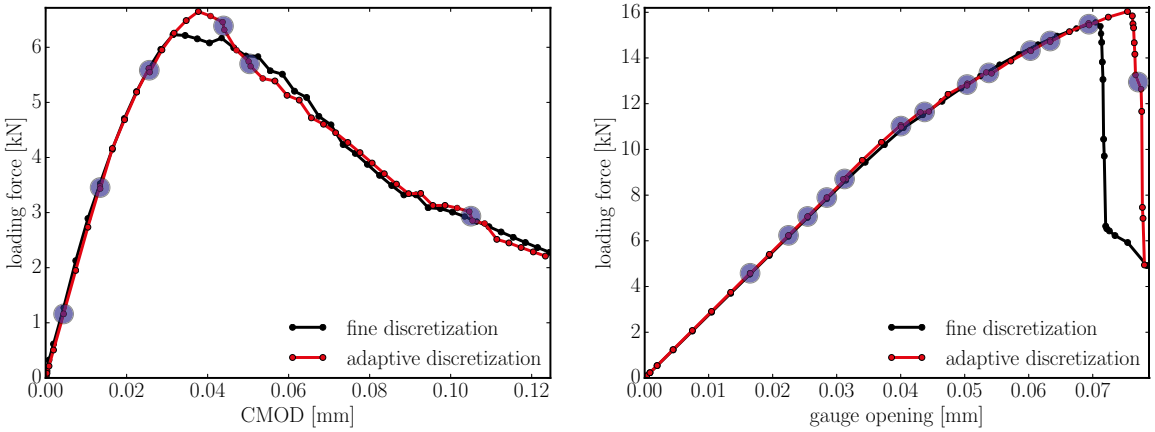

Figure 8: Comparison of responses of beams with notch (left) and without notch (right) with fine discretization and with adaptive discretization refinement.

also different response. Further simulations will be performed to show whether the mean value and also variance of the peak load from the adaptive model matches those from the reference model.

Finally, Fig. 6 shows crack patterns developed in both models. Three stages - initial, at the peak load and at the end of the simulation - are presented. Number of DOF at each stage is listed bellow the figures. Finely discretized model has about 50000 DOF during the whole simualtion. Adaptive models starts at 9000 (approx. 1/8 as the $l_{\min}$ is doubled) but number of DOF increases during refinements.

7 CONCLUSIONS

- The adaptive discretization refinement for discrete meso-scale models of fracture was presented. The adaptivity is performed in model of random geometry created via Voronoi tessellation.
- The developed approach was verified on simulations of beams subjected to three-point bending. Significant time savings were achieved.
- Presented concept of adaptivity can be successfully applied in problems where material non-linearity is localized into small portion of the modeled element, but the location of that region is not known in advance.

ACKNOWLEDGEMENT

The financial support provided by the Czech Science Foundation under project No. 15-19865Y is gratefully acknowledged.

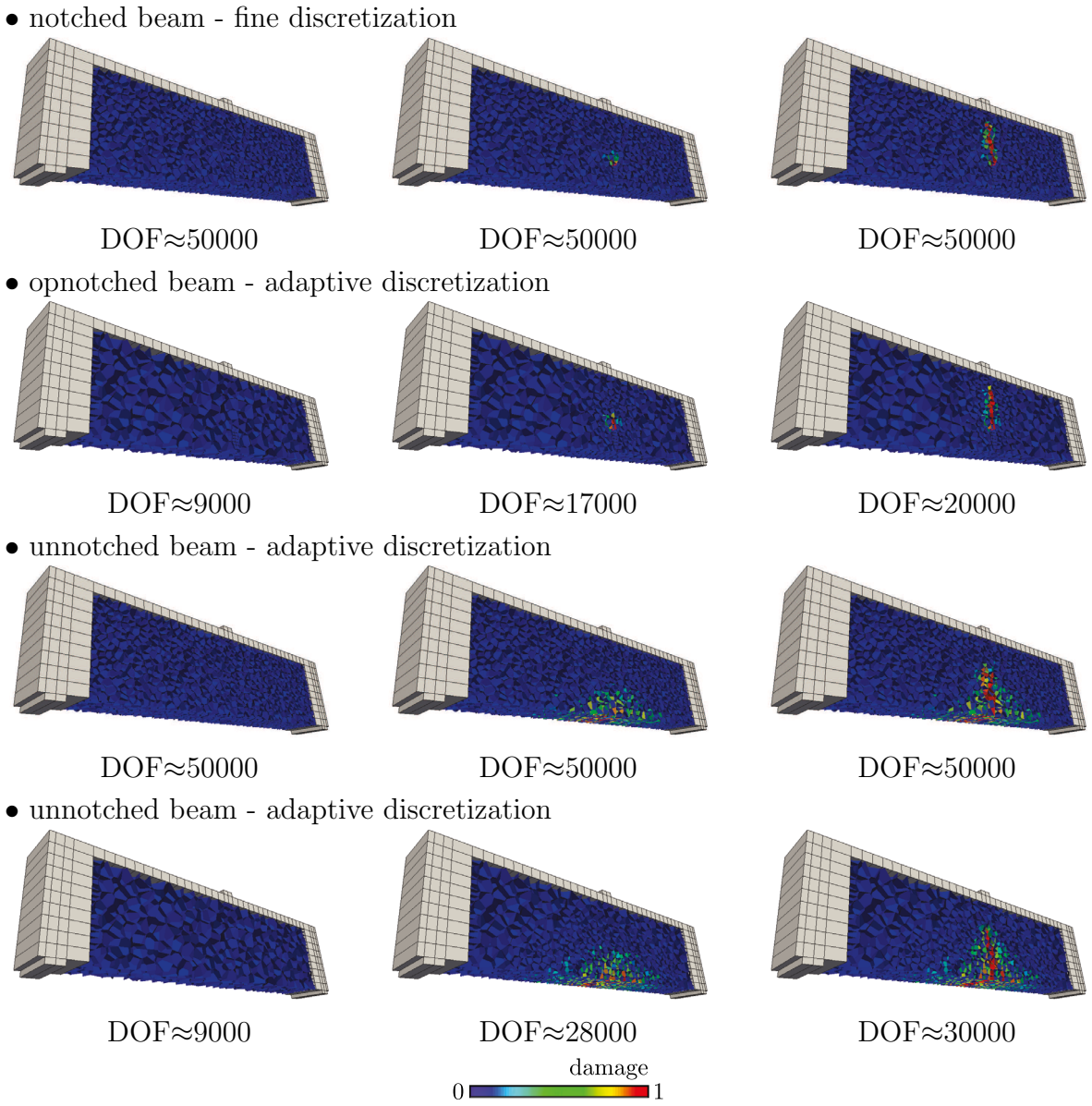

Figure 9: Damage patterns developed during simulations. Two stages are shown - in the solution step when the maximum load war reached and at the end of the simulation. Approximate number of DOF in the simulation stages is written bellow.

REFERENCES

[1] J. E. Bolander and S. Saito. Fracture analyses using spring networks with random geometry. *Eng. Fract. Mech.*, 61:1569–591, 1998. ISSN 0013-7944. doi: 10.1016/S0013-7944(98)00069-1.

[2] Y. H. Gedik, H. Nakamura, Y. Yamamoto, and M. Kunieda. Evaluation of three-dimensional effects in short deep beams using a rigid-body-spring-model. *Cement Concrete Comp.*, 33:978–991, 2011. ISSN 0958-9465.

[3] Jan Eliáš and Jia-Liang Le. Modeling of mode-i fatigue crack growth in quasibrittle structures under cyclic compression. *Eng. Fract. Mech.*, 96:26–36, 2012. ISSN 0013-7944. doi: http://dx.doi.org/10.1016/j.engfracmech.2012.06.019.

[4] J. Bolander, T. Shiraishi, and Y. Isogawa. An adaptive procedure for fracture simulation in extensive lattice networks. *Eng. Fract. Mech.*, 33:325–334, 1996. ISSN 0013-7944. doi: 10.1016/0013-7944(95)00200-6.

[5] Annika Sorg and Manfred Bischoff. Adaptive discrete-continuous modeling of evolving discontinuities. *Eng. Computation.*, 31(7):1305–1320, 2014. doi: 10.1108/EC-03-2013-0072.

[6] Gianluca Cusatis, Daniele Pelessone, and Andrea Mencarelli. Lattice discrete particle model (LDPM) for failure behavior of concrete. I: Theory. *Cement Concrete Comp.*, 33(9):881–890, 2011. ISSN 0958-9465.

[7] Gianluca Cusatis, Zdeněk P. Bažant, and Luigi Cedolin. Confinement-shear lattice CSL model for fracture propagation in concrete. *Comput. Method. Appl. M.*, 195 (52):7154–7171, 2006. ISSN 0045-7825.

[8] Gianluca Cusatis and Luigi Cedolin. Two-scale study of concrete fracturing behavior. *Eng. Fract. Mech.*, 74(12):3–17, 2007. ISSN 0013-7944.

[9] Gianluca Cusatis, Andrea Mencarelli, Daniele Pelessone, and James Baylot. Lattice discrete particle model (LDPM) for failure behavior of concrete. II: Calibration and validation. *Cement Concrete Comp.*, 33(9):891–905, 2011. ISSN 0958-9465. doi: http://dx.doi.org/10.1016/j.cemconcomp.2011.02.010.

[10] Jan Eliáš, Miroslav Vořechovský, Jan Skoček, and Zdeněk P. Bažant. Stochastic discrete meso-scale simulations of concrete fracture: comparison to experimental data. *Eng. Fract. Mech.*, 135:1–16, 2015. ISSN 0013-7944. doi: 10.1016/j.engfracmech.2015.01.004.

[11] Christian G. Hoover, Zdeněk P. Bažant, Jan Vorel, Roman Wendner, and Mija H. Hubler. Comprehensive concrete fracture tests: Description and results. *Eng. Fract. Mech.*, 114(0):92–103, 2013. ISSN 0013-7944. doi: http://dx.doi.org/10.1016/j.engfracmech.2013.08.007.

[12] Christian G. Hoover and Zdeněk P. Bažant. Comprehensive concrete fracture tests: Size effects of types 1 & 2, crack length effect and post-peak. *Eng. Fract. Mech.*, 110:281–289, 2013. ISSN 0013-7944. doi: http://dx.doi.org/10.1016/j.engfracmech.2013.08.008.

[13] Roman Wendner, Jan Vorel, Jovanca Smith, Christian G. Hoover, Zdeněk P. Bažant, and Gianluca Cusatis. Characterization of concrete failure behavior: a comprehensive experimental database for the calibration and validation of concrete models. *Mat. Struct.*, pages 1–24, 2014. ISSN 1359-5997. doi: 10.1617/s11527-014-0426-0.

[14] Jacky Mazars. *Application de la mécanique de l'endommagement au comportement non linéaire et à la rupture du béton structure.* Ph.d. thesis, Université de Paris, 1984.